ROYAL SOCIETY
OF CHEMISTRY

PAPER

Check for updates

Development of a spin selective electrocatalyst platform and its use to study spin-polarization and d-orbital occupancy effects in oxygen evolution reaction electrocatalysts

Meera Joy, [ID] Brian P. Bloom, [ID] Keerthana Govindaraj, [ID] Joseph A. Albro, [ID] Aravind Vadakkayil [ID] and David H. Waldeck [ID] *

We describe a polymer–catalyst platform that uses spin-polarized electron currents, recently reported to improve the efficiency of the oxygen evolution reaction (OER), in combination with transition metal-oxide catalysts to enhance the efficiency of their OER electrocatalysis. We describe the creation of an electrode coated with a chiral conjugated polymer film which acts as a spin transport layer and ensures that the anodic reaction proceeds with a spin bias. Systematic studies on a series of transition metal oxide catalysts demonstrate that spin selectivity improves catalytic efficiency irrespective of the catalyst's position on a 'volcano' plot and that the benefit correlates with the expected number of unpaired d-orbital electrons in the catalyst. These studies demonstrate a promising electrode scaffold for investigating the role of electron spin currents in chemical reactions.

1 Introduction

The oxygen evolution reaction (OER) is an important bottleneck for energy storage devices such as metal air batteries, water electrolysis, and regenerative fuel cells.[1,2] It is a limiting reaction in the process of generating molecular oxygen through redox chemistry, such as the oxidation of water during oxygenic photosynthesis, electrolysis of water into oxygen and hydrogen, and electrocatalytic oxygen evolution from oxides and oxoacids.[3] Thus, it is important from both a fundamental perspective and for applications.[4] The electrochemical OER proceeds through a complex set of four proton-coupled electron transfer steps, with adsorbed *OH, *O, and *OOH radical intermediates, to generate diatomic oxygen, which exists as a triplet in its ground state.[5,6]

To rationalize the activity of electrocatalysts in a family of catalyst materials, researchers often adopt Sabatier's principle, *i.e.* the notion that the binding energy of reaction intermediates should be neither too strong nor too weak to facilitate a reaction.[7] In the case of OER this is reflected in the binding energies of oxo and hydroxyl intermediates ($\Delta G_O - \Delta G_{OH}$) and manifests as a 'volcano plot', in which the apex of the plot is the voltage nearest to the ideal thermodynamic potential for catalysis; *i.e.*, smallest overpotential.[8,9] In addition to this energy effect, researchers have demonstrated that electrocatalytic activity is impacted by electron orbital and spin effects, *e.g.* engineering e_g

electron filling in LaCoO$_3$-based electrocatalysts,[10] regulating e_g electron filling and spin states through sulfur[11] and fluorine[12] atom doping, and Zn^{2+} substitution in spinel Co$_3$O$_4$ catalysts.[13]

While considerable progress has been made using these approaches, recent studies demonstrate that spin polarizing reaction intermediates during OER can also improve catalytic activity. Spin polarization during catalysis has been achieved primarily through two approaches: (1) application of an external magnetic field on a paramagnetic or ferromagnetic catalyst[14–21] and (2) use of chiral catalysts that display the chiral-induced spin selectivity (CISS) effect.[22–26] The CISS effect has been used in a number of different ways to boost OER efficiency,[27–32] including (photo-) electrocatalytic water splitting, in which covering the anode with chiral molecules increases the overall cell performance.[33–35] Note, that other methods for spin-polarizing electron currents during OER have also been explored, including the implementation of 'spin-pinning' layers or spin-polarized defect sites, the exploitation of spin-selective carrier transport, and the introduction of a chiral bias using molecular additives, among others; however these methods are less well studied.[15,36–40] The spin-polarization enhanced OER is often attributed to changes in the transition state energies of reaction intermediates, as well as reaction pathways, compared to systems with unpolarized catalysts.[14–16] Both the strength of an applied external magnetic field on a ferromagnetic catalyst and the 'degree of chiral imprinting' on a chiral catalyst can affect the magnitude of spin polarization and consequently the improvement in OER performance.[41,42] While a large breadth of studies demonstrate that spin polarization enhances OER,[43]

Chemistry Department, University of Pittsburgh, Pittsburgh, Pennsylvania 15260, USA. E-mail: dave@pitt.edu

36720 | *J. Mater. Chem. A*, 2025, **13**, 36720–36728

This journal is © The Royal Society of Chemistry 2025

a thorough understanding of how these effects coincide, or not, with traditional methods for predicting catalyst activity, *i.e.*, 'volcano' plots, is unknown.

This work distinguishes the effect of the spin-polarized current from other contributions to catalytic activity by performing a systematic study in which the same spin polarization is transferred to different catalysts. To this end, we developed a chiral scaffold that delivers spin-polarized electron currents to OER catalysts and probe the impact of spin polarization on a series of achiral metal-oxide catalysts. Note this is operationally a similar approach to that reported previously using chiral helicenes with Ni,[38] however here we use polyaniline (PANI) as a robust and conductive scaffold that can be made chiral or achiral. This approach circumvents the need to create ferromagnetic catalysts or chiral catalysts, rather the same catalyst can be studied both with and without spin-polarizing electron currents.

Previous studies have shown that PANI operates as a successful catalyst support for chemical reactions[44–46] and, when made chiral using dopants, functions as an efficient spin filter.[47–49] By combining these two attributes, we demonstrate the fabrication of a flexible catalyst support platform that: (1) can incorporate a wide array of metal catalysts through drop casting nanoparticles or through electrodeposition,[50–53] to form PANI-catalyst composites and (2) owing to the robust pH and potential stability of PANI, is capable of operating under basic and acidic conditions at both high anodic and cathodic potentials. Because the chiral polyaniline thin film is placed between the catalyst and the anode, it serves as a 'spin transport layer', *i.e.* it abstracts (transmits) spin-polarized electrons from (to) the electrocatalyst thereby leading to spin alignment of reaction intermediates on the catalyst surface. Note that, the emergence of spin-polarized electron transport through the chiral polyaniline does not rely on magnetic properties of the catalyst. Previous studies have shown that chiral molecules, materials, and their assemblies, can manifest CISS without external magnetic components or magnetic fields.[54–56]

Below we apply this unique platform to examine how the OER activity of simple transition-metal oxide catalysts changes on spin-polarizing (chiral) polyaniline films *versus* on nonspin-polarizing (racemic) polyaniline films. Our findings show that the spin-polarizing catalyst scaffold improves OER activity and implies that spin acts as an additional design feature that operates in concert with traditional activity metrics, *e.g.* volcano plots. While the focus of the studies herein is on OER, the versatility of the chiral PANI-catalyst support represents a viable system for studying the effect of spin in other chemical reactions.

2 Experimental section

2.1. Materials

All commercial materials and solvents were used without further purification unless otherwise indicated. Sodium borohydride, Nafion perfluorinated resin solution, *S*-camphor sulfonic acid, *R*-camphor sulfonic acid, *p*-phenylene diamine, aniline, nickel(II) sulfate hexahydrate, iron(II) sulfate heptahydrate, copper(II) sulfate pentahydrate, cobalt(II) sulfate

heptahydrate, iridium(IV) oxide, ruthenium(IV) oxide, titanium(IV) oxide, sodium perchlorate monohydrate and urea were purchased from Sigma-Aldrich. HCl was purchased from Fischer chemicals. KOH, H_2SO_4 were purchased from Fisher Scientific. Sodium nitrite and boric acid were purchased from J. T. Baker and Fisher Bio-Reagents respectively.

2.2. Preparation of spin transport layer

Substrates were fabricated by e-Beam deposition of 3 nm Ti and 10 nm Au onto quartz substrates, using a Plassys Electron Beam Evaporator MEB550S. The polyaniline film was then prepared by two sequential steps: covalent modification of an electrode through grafting, followed by electropolymerization of aniline. To ensure the stability of the chiral support, the electrode surface was molecularly grafted, following a previously published procedure,[57] through an *in situ* generated diazonium salt. The 4-aminophenyl diazonium salt was formed by reacting 5 mM *p*-phenylene diamine with 1 equivalent of sodium nitrite in a 0.5 M HCl solution. Reduction of the salt under moderate potentials (−0.4 V *vs.* Ag/AgCl) formed a metal–carbide bond and the grafted electrode was then sonicated for 5 minutes to remove any unbound molecules. The resulting amine-terminated modified electrode surface now acts as an initiation site for the polymerization of aniline.[58] Electropolymerization of aniline was performed in the presence of *R*- or *S*-camphor sulfonic acid (CSA), a counterion which binds to the backbone of the polymer, to form chiral *R*-PANI or *S*-PANI. Conversely, polymerization in the presence of racemic CSA resulted in no net chirality of the resulting polymer, *i.e.* a null response in the circular dichroism was observed. The PANI layer was prepared through electropolymerization in a 0.2 M aniline and 1 M *S*-, *R*-, or *rac*-CSA solution under potentiostatic conditions (0.75 V) until the desired thickness (*ca.* 100–120 nm) was achieved.

2.3. Electrodeposition of metal electrocatalysts

The electropolymerized films were de-doped by immersing them in 0.5 M ammonium hydroxide solution for 20 minutes and then thoroughly rinsing with deionized water. Catalysts were then deposited onto the PANI films through electrodeposition. For Ni catalysts,[59] a solution of 0.01 M nickel(II) sulfate hexahydrate in 0.01 M boric acid and 1×10^{-6} M H_2SO_4 at −1.4 V *vs.* Ag|AgCl for 25 seconds was used. For Co catalysts,[53] a solution of 0.01 M cobalt(II) sulfate heptahydrate in 0.01 M boric acid and 1×10^{-6} M H_2SO_4 at −1.4 V *vs.* Ag|AgCl for 25 seconds was used. For Fe catalysts, a solution of 0.01 M iron(II) sulfate heptahydrate in 0.01 M boric acid and 1×10^{-6} M H_2SO_4 at −1.4 V *vs.* Ag|AgCl for 25 seconds was used. For Cu catalysts,[60] a solution of 0.01 M copper(II) sulfate pentahydrate and 0.1 M sodium perchlorate monohydrate at −1.2 V *vs.* Ag/AgCl for 25 seconds was used.

2.4. Preparation of catalyst ink solutions

IrO_2 and RuO_2 ink solutions were prepared in 10 μL of 5 wt% Nafion and 1 mL of a water/ethanol solution (1 : 1 v/v). The mixture was sonicated for 15 minutes and then 5 mg of the catalyst, was added to the solution. An additional 30 min of sonication was performed and a 2 μL aliquot of the solution was

This journal is © The Royal Society of Chemistry 2025

J. Mater. Chem. A, 2025, **13**, 36720–36728 | **36721**

drop cast onto 0.07 cm^2 glassy carbon electrode coated with the PANI film. The TiO$_2$ ink solution was prepared by sonicating 3 mg of TiO$_2$ in 30 μL of 5 wt% Nafion and 1 mL of a water/ethanol solution (3 : 1 v/v) for 30 minutes.

2.5. Characterization

Circular dichroism measurements were performed using a Jasco J810 CD spectrometer with an integration time of 4 s and a bandwidth of 1 nm. UV-visible absorbance measurements were made using an Agilent (Model 8453) spectrometer. X-ray photoelectron spectroscopy (XPS) measurements were performed using a PHI Genesis system at a 55 eV pass energy, 20 ms dwell time, and with a 0.1 eV increment. All of the data were charge referenced to the c–c peak of adventitious carbon, 284.8 eV. SEM images were collected on a ZEISS Sigma 500 VP scanning electron microscope (SEM) at a working distance of 3–6 mm and an accelerating voltage of 3 kV. The mc-AFM measurements were carried out on a Bruker Dimension Icon atomic force microscope. The PANI films were electrodeposited on 100 nm Au/5 nm Ti/Si wafer. To ensure that the thickness of the electrodeposited film was the same for R- and S-PANI films, surface profilometry measurements (KLA-Tencor Alpha-Step IQ Surface Profiler) were performed following electropolymerization. To decrease surface roughness effects, which can arise with thicker films, thinner PANI films were used to perform the mcAFM measurements; the average thickness of R-PANI films (14.1 ± 2.2 nm), S-PANI (12.9 ± 2.7 nm), and rac-PANI films (12.7 ± 2.3 nm) were within error of each other. The mc-AFM measurements were performed using a ferromagnetic CoCr tip (HQ:NSC18/Co-Cr, MikroMasch) with a force constant of 2.8 N m^{-1}. The ferromagnetic AFM probes were magnetized by placing the AFM probe (tip apex facing upwards) onto the corresponding pole of a magnet. Measurements were made by collecting current–voltage (I–V) curves at different regions of the film (c.a. 60 spots) for a North magnetized tip, followed by ∼60 different regions with a South magnetized tip, and then lastly another ∼60 regions with a North magnetized tip. Only data in which the first North magnetized tip is within the 95% confidence interval of the second North magnetized tip measurement were considered viable.

2.6. Electrochemical measurements

Electrochemical measurements were carried out using either a 618 B or 430 A potentiostat (CH Instruments). The reference electrode was a saturated KCl Ag|AgCl (CH Instruments) and the counter electrode was a platinum wire. Linear sweep voltammetry (LSV) experiments for all of the catalyst materials were collected at a scan rate of 10 mV s^{-1}. The electrochemical results reported in this work were all iR compensated.

3 Results and discussion

3.1. Deposition and characterization of polyaniline spin transport layer

To form catalyst-coated polyaniline thin films, a three-step process was used; see Fig. 1 for a schematic of the process.

Briefly, bi-/tri-layer polymer nucleation sites were first chemically grafted onto the electrode surface through reduction of an in situ generated diazonium salt (i). See SI for characterization of the grafted surface. Next, aniline was electropolymerized onto the electrode (ii). Fig. 1b shows representative absorbance spectra of PANI films prepared in the presence of S-camphorsulfonic acid (S-PANI, blue), R-camphorsulfonic acid (R-PANI, green), and racemic-camphorsulfonic acid (rac-PANI, purple). The spectral features at 330 nm and 590 nm are characteristic of the emeraldine base form of polyaniline and have previously been assigned to a benzenoid π–π* transition and the quinoid groups in the polymer backbone, respectively.[61] Films of thickness ranging from 80–100 nm were used for the experiments, and the thickness was controlled through the polymerization time. A calibration curve for determining the thickness from the absorbance is shown in Fig. S2. In the presence of chiral camphorsulfonic acid dopants, the films manifest chiroptical properties consistent with that shown in other works.[62] Fig. 1c shows corresponding circular dichroism spectra of the resulting S-PANI (blue) and R-PANI thin films (green) in which mirror image Cotton effects are observed at the electronic transitions of the polymer, indicating successful chirality induction in the films prepared with chiral dopants. Conversely, a null circular dichroism response was observed for the rac-PANI (purple).

To demonstrate that chiral PANI thin films act as spin transport layers, magnetic conductive atomic force microscopy (mcAFM) was performed using a magnetized ferromagnetic AFM tip. Because of the CISS effect, the conduction of charge current is favored for one electron spin orientation, i.e. tip magnetization, over that of the other.[63,64] Fig. S3 shows average I–V curves measured for R-, S-, and rac-PANI with a South and North magnetized ferromagnetic AFM tip. For S-PANI films a higher current is observed when the electron spin is aligned antiparallel to its momentum whereas the opposite is observed for R-PANI films, a higher current is observed when the electron spin is aligned parallel to its momentum. Conversely, for rac-PANI no difference in I–V response with magnetization was observed. The asymmetry in current response was used to obtain a spin polarization $\frac{I_{parallel} - I_{antiparallel}}{I_{parallel} + I_{antiparallel}} \times 100\%$ and the data are plotted in Fig. 1d as a function of applied bias. The equal and opposite average spin polarization for S-PANI (−34.66 ± 9.5%) and R-PANI (30.52 ± 8.7%) is a hallmark of the CISS effect. Note, the spin polarization values observed in this work are in reasonable agreement with other literature reports for chiral PANI.[44–46]

3.2. Oxygen evolution reaction with electrodeposited catalysts

Next, we compared the OER activity of catalysts deposited on R- and S-PANI thin films, which spin polarize charge currents, to rac-PANI thin films, which do not. Two main methods were used for deposition of the catalysts (step (iii) in Fig. 1a): (1) electrodeposition of catalyst nanoparticles onto the PANI films, and (2) drop casting of commercially available nanoparticle catalysts. Details of catalyst preparation are provided in the

36722 | J. Mater. Chem. A, 2025, 13, 36720–36728

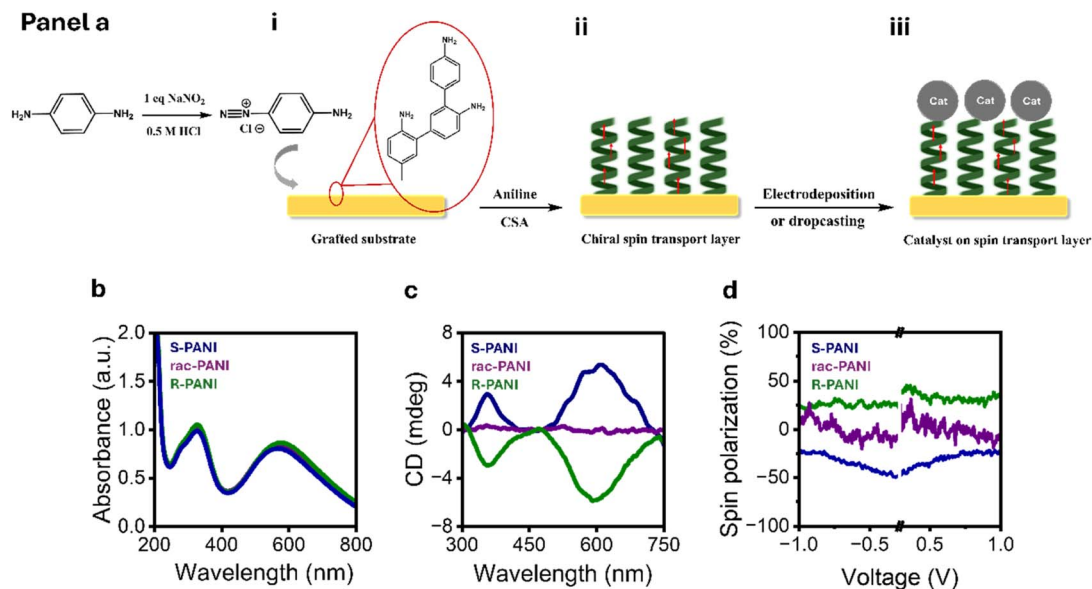This journal is © The Royal Society of Chemistry 2025

Fig. 1 Panel (a) shows a schematic diagram for the preparation of chiral polyaniline spin transport layers by electropolymerization on a chemically derivatized substrate: (i) a diazonium salt was generated *in situ* and its reduction on the surface of electrode forms a metal–carbide bond, (ii) electropolymerization of aniline onto the chemically derivatized electrode surface in the presence of camphor sulfonic acid was used to produce a chiral polyaniline film, and (iii) the OER electrocatalyst material was deposited on the chiral polymer film, either by electrodeposition or by drop casting. Absorbance (b) and circular dichroism spectra (c) of electropolymerized *S*-PANI (blue), *R*-PANI (green), and *rac*-PANI (purple) films. Spin polarization (d) of *S*- (blue), *R*- (green), and *rac*-PANI (purple) films were determined using mcAFM as a function of applied voltage.

Experimental section. Initial studies investigated nickel, iron, cobalt, and copper catalysts formed from an acidic metal salt solution under reductive potentials (see Experimental section for detailed procedures). Fig. S4 shows that the chiro-optical properties of the underlying PANI layer persist through the electrodeposition and OER electrolysis. Note that, X-ray
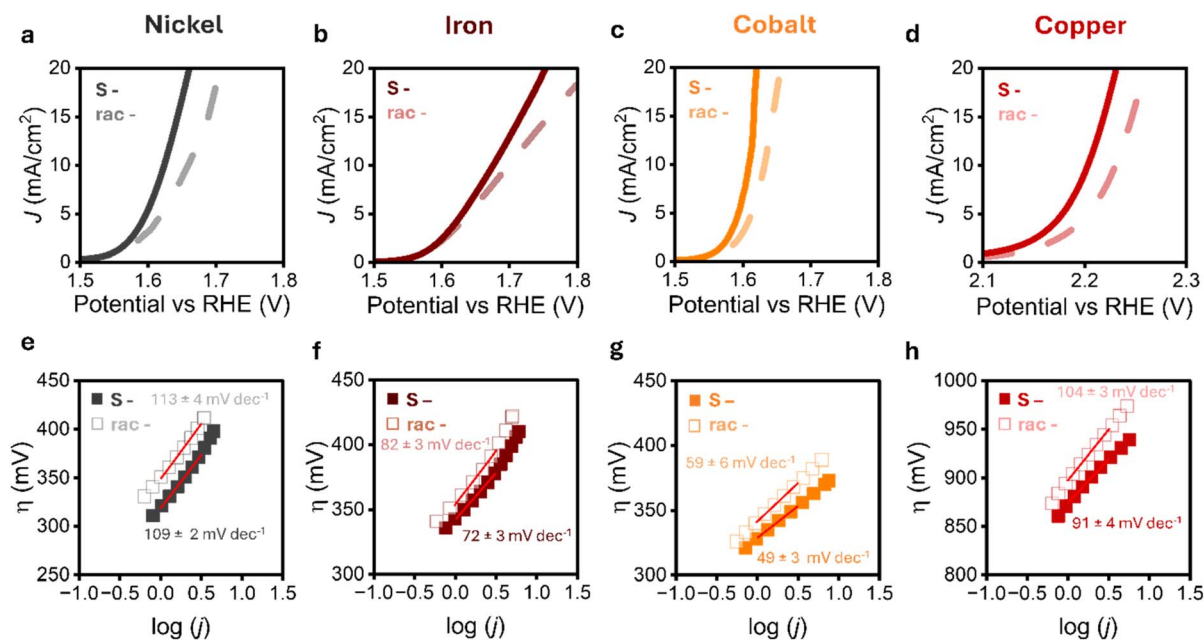

Fig. 2 Panels (a–d) show linear sweep voltammograms of nickel (grey), iron (brown), cobalt (orange) and copper (red) based metal-oxide catalysts electrodeposited on *S*-PANI (solid line) and *rac*-PANI (dotted line). These data represent the average of three separately prepared electrodes. Panels (e–h) show corresponding Tafel plots of the catalysts deposited on *S*-PANI (filled squares) and *rac*-PANI films (open squares). These data represent the average from three separately prepared electrodes and the error in slope is associated with the standard deviation of the mean.

This journal is © The Royal Society of Chemistry 2025

J. Mater. Chem. A, 2025, 13, 36720–36728 | 36723

photoelectron spectra (Fig. S5 and S6) show that the electro-deposited material is fundamentally equivalent when deposited on *R*-, *S*-, and *rac*-PANI; *i.e.*, the elemental composition and oxidation state distribution of the metals are within error of each other. In addition, scanning electron micrographs (Fig. S7) indicate that the catalyst size and morphology are also similar. These characterization data imply that the morphological features and composition of the catalyst nanoparticles do not depend on whether the underlying PANI layer is chiral or racemic.

Fig. 2a–d show linear sweep voltammograms, under potential conditions at which OER occurs, for nickel (grey), iron (brown), cobalt (orange), and copper (red) based metal-oxide catalysts deposited on *rac*-PANI (dashed line) and *S*-PANI (solid line) thin films. For each catalyst type a decrease in the reaction overpotential, η, is observed on *S*-PANI thin films compared to *rac*-PANI. In addition, the catalysts on the chiral *S*-PANI films (filled squares) show a decrease in the Tafel slope compared to the same catalysts on the *rac*-PANI films (open squares); see Fig. 2e–h. Note that measurements on catalysts deposited on *R*-PANI thin films exhibit similar catalytic behavior to that of *S*-PANI thin films and are shown in Fig. S8–S10. Collectively, these data demonstrate that catalysts placed on thin film scaffolds that spin-filter charge current, *i.e.* chiral PANI, exhibit improved OER kinetics compared to films which do not spin-filter the electron current, *rac*-PANI. To ensure that the improved performance is not associated with changes in the electrochemical surface area double layer capacitance measurements were performed; see Fig. S11 and corresponding discussion in the SI.

3.3. Oxygen evolution reaction with commercial catalysts

A similar improvement in OER activity was also observed for drop-cast Nafion ink suspensions containing commercially available nanoparticle catalysts, namely IrO_2 and RuO_2 on chiral PANI thin films over *rac*-PANI films. Fig. 3a and b show linear sweep voltammograms that display a decrease in reaction overpotential of catalysts deposited on *S*-PANI (solid line) compared to *rac*-PANI films (dashed line), and Fig. 3d and e show a decrease in the Tafel slope of IrO_2 and RuO_2 catalysts deposited on *S*-PANI (filled squares) compared to *rac*-PANI (open squares) films. Note that, Fig. S8–S10 show measurements made on *R*-PANI thin films in which a similar performance to *S*-PANI films is observed. Interestingly, measurements made using ink suspensions comprising TiO_2 catalysts did not exhibit changes, outside of statistical error, in overpotential or Tafel slope, when deposited on *S*-PANI films and *rac*-PANI films (see Fig. 3c and f). Note that similar to the case of electro-deposited catalysts, the electrochemical surface area of drop cast ink suspensions, determined through double layer capacitance, confirms that the comparison between *S*-PANI and *rac*-PANI films is not influenced by differences in electrochemically active surface area (Fig. S11).

3.4. Electroactive forms of explored catalysts

To understand these data, consider that the most likely forms of the catalysts are oxyhydroxides for Fe, Co, and Ni,[65] and IrO_2, RuO_2,[66] CuO,[67] and TiO_2 (ref. 9) for the others, under the voltage and pH conditions for the OER in this study. Note that this assignment of the catalytic form is consistent with *ab initio*
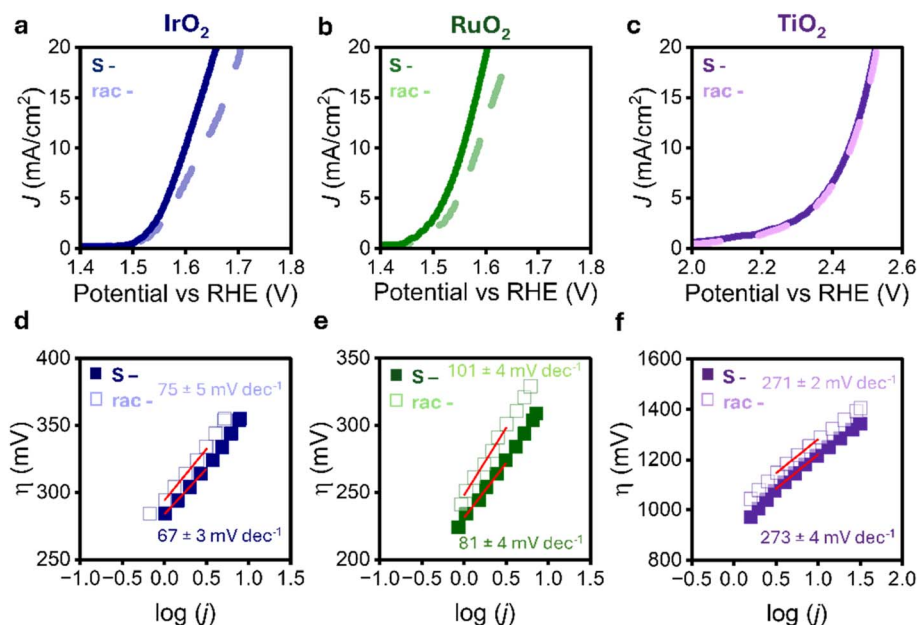

Fig. 3 (a–c) shows the linear sweep voltammograms of IrO_2 (blue), RuO_2 (green), and TiO_2 (purple) nanoparticle catalysts in Nafion drop cast onto chiral *S*-PANI (solid line) and achiral *rac*-PANI (dashed line) in a 1 M KOH electrolyte. These data represent the average of three separately prepared electrodes. Panels (d–f) show Tafel plots and corresponding slopes for IrO_2 (blue), RuO_2 (green), and TiO_2 (purple) drop cast onto chiral (filled symbol) and racemic (open symbol) PANI films. These data represent the average from three separately prepared electrodes and the error in slope is associated with the standard deviation of the mean.

36724 | *J. Mater. Chem. A*, 2025, **13**, 36720–36728

This journal is © The Royal Society of Chemistry 2025

Table 1 Comparison of the reaction overpotential, η, and Tafel slope, b, for catalysts deposited on *S*-PANI and *rac*-PANI to that published previously in the literature on the same catalysts. The data points represent the average from three independently prepared electrodes, and the error corresponds to the standard deviation from the mean

| Catalyst | *S*-PANI | | *rac*-PANI | | Literature | | |
	η (mV)	b (mV dec^{-1})	η (mV)	b (mV dec^{-1})	η (mV)	b (mV dec^{-1})	Ref.
NiOOH	394 ± 3	109 ± 2	429 ± 2	113 ± 4	533–620	105	59 and 73
FeOOH	416 ± 2	72 ± 3	449 ± 2	82 ± 3	450	68–100	73
CoOOH	380 ± 7	49 ± 3	407 ± 8	59 ± 6	370–430	69–95	74
CuO	969 ± 3	91 ± 4	1006 ± 4	104 ± 3	400–600	89–110	67, 75 and 76
IrO$_2$	369 ± 7	67 ± 3	402 ± 3	75 ± 5	340	93	36 and 77
RuO$_2$	326 ± 8	81 ± 4	355 ± 7	101 ± 4	366	104	36 and 78
TiO$_2$[a]	1213 ± 5	273 ± 4	1223 ± 5	271 ± 6	1250	—	9

[a] Values reported at a current density of 0.1 mA cm^{-2} to match the literature reported overpotential values at the given current density.

calculations, as well as Pourbaix diagrams,[68–72] and were substantiated electrochemically. For example, Fig. S12 shows oxidation peaks associated with the electrochemical conversion of Ni^{2+} to Ni^{3+} for nickel-based catalysts and Co^{2+} to Co^{3+} for cobalt-based catalysts that occur prior to OER currents. Table 1 summarizes the reaction overpotentials (η) and Tafel slopes from measurements of different catalysts on *S*-PANI and *rac*-PANI electrodes, and it compares our findings to previous measurements published in the literature, where possible. To ensure valid comparisons, we cite works that operate under similar reaction and solution conditions to that reported here. The overpotential and Tafel slope of catalysts deposited on *rac*-PANI are in most instances comparable to that of achiral catalysts reported in the literature and highlight that resistance associated with transport through the PANI film is not likely a contributing factor under these measurement conditions. In addition, these comparisons corroborate the assumption about the catalyst oxidation state. The variation in activity for different catalysts depends upon multiple factors, and so a platform that delivers similar spin-polarized electron currents is essential for providing a fundamental understanding about the effect of spin on OER.

3.5. Trends in spin promoted oxygen evolution reaction

To examine how spin polarization fits within the context of Sabatier's principle, we have constructed a volcano plot comprising the different catalysts investigated in this study. Fig. 4a plots the experimentally determined reaction overpotential at 10 mA cm^{-2} for catalysts deposited on *S*-PANI thin films (filled symbol) and *rac*-PANI films (open symbol). Note that, the free energies of the adsorbed reaction intermediates ($\Delta G_O - \Delta G_{OH}$) were taken from previous calculations[9,59–61] on catalysts of the form expected to be present during OER under these potential and pH conditions. An approximately 20–40 mV reduction in overpotential is observed for all of the measured catalysts, with the exception of TiO$_2$ for which no improvement was observed. Note that the reduction in overpotential is independent of whether the catalyst is on the left or right side of the apex of the volcano plot. These findings suggest that spin alignment of
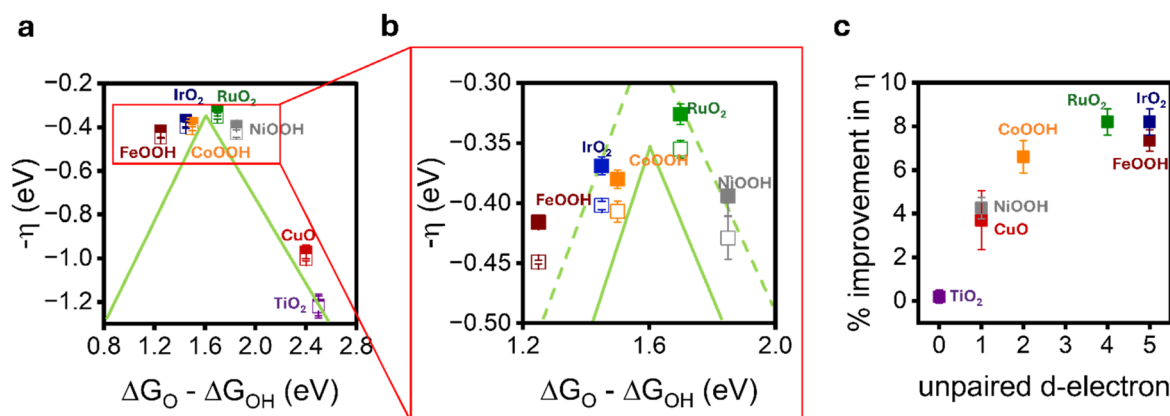
Fig. 4 (a) Relationship between the OER overpotentials, η, at 10 mA cm^{-2} and the difference in reaction intermediate adsorption energies, ($\Delta G_O - \Delta G_{OH}$), for catalysts prepared on *S*-PANI (filled symbols) and *rac*-PANI films (open symbols). The green fitted line is adapted from ref. 9. Panel (b) shows a zoomed in region near the apex of the volcano plot. Note that the free energies of the adsorbed reaction intermediates ($\Delta G_O - \Delta G_{OH}$) values were adapted from ref. 9, 59, 60, and 61 on catalysts of the form expected to be present during OER collected under the experimentally applied potential and pH conditions. Panel (c) shows the correlation between the percent improvement in reaction overpotential of *S*-PANI films to *rac*-PANI films to the number unpaired electrons in the d-orbitals of the catalyst's oxidation state formed during OER. The data points represent the average from three independently prepared electrodes, and the error bars correspond to the standard deviation to the mean.

This journal is © The Royal Society of Chemistry 2025

J. Mater. Chem. A, 2025, **13**, 36720–36728 | **36725**

reaction intermediates, imparted through a spin transport layer, is not changing the free energies of the adsorbates, but instead represents an additional control variable that can improve catalysis. Fig. 4b shows an expanded view near the apex of the volcano plot, and the spin promoted shift in overpotential values is indicated by the dashed green line. Previous studies have reported that the transition state energies for different steps in the OER are strongly affected by spin alignment on the catalyst surface;[79,80] our hypothesis that selective spin injection into an electrocatalyst (because of CISS) should improve reaction efficiency, presumably by polarizing reaction intermediates and promoting the formation of triplet oxygen, is corroborated by these data. It is important to stress that the chiral spin transport layer used in this work is not the best, exhibiting a modest spin polarization of ~35%, and that a more significant improvement would likely be observed with a better spin transport layer.

Interestingly, the percent improvement in overpotential $((\eta_{rac} - \eta_S)/\eta_{rac} \times 100\%)$ correlates with the expected number of unpaired electrons in the catalyst's d-orbitals (Fig. 4c). An increase in the number of unpaired electrons shows a more favorable response to the spin selective transport emanating from chiral PANI for improving the OER. Note that, the TiO_2 catalysts do not possess any unpaired d-orbital electrons at these pH and potential conditions, and no improvement in the OER with chiral PANI is observed. In other CISS studies researchers have shown the importance of unpaired spins in electrode materials to promote long-range spin-selective transport,[81,82] and it may be that a similar mechanism operates here. Concerning whether one or more of the catalyst materials becomes magnetized during the OER reaction, the data presented here is moot. Such a claim would require that the magnetic properties of the electrode assemblies be measured *in operando* and is beyond the scope of this work.

4   Conclusions

This work developed a chiral polymer scaffold as a spin-transport layer and examined its use for enhancing the performance of simple transition metal oxide catalysts in the OER reaction, which is known to be sensitive to the electron spin. We showed that use of the chiral polymer scaffolds leads to a decreased reaction overpotential and Tafel slope for the OER catalysis compared to analogous nonpolarizing (achiral) scaffolds for the same catalyst. Through investigation of a series of transition metal oxide catalysts, we showed that spin polarization can improve the reaction overpotential beyond the conventional constraints set forth by considering the adsorption energies of reaction intermediates alone. Interestingly, the OER improvement correlates with the expected number of unpaired d-electrons in the catalyst, however the cause of this correlation requires further work for full elucidation. This work demonstrates that a chiral catalyst scaffold can be used to enhance spin-dependent electrocatalysis.

Author contributions

Meera Joy: formal analysis, investigation, writing – original draft; Brian P. Bloom: XPS, SEM characterization, writing (editing and review); Keerthana Govindaraj: mcAFM measurements; Joseph A. Albro: AFM topography imaging; Aravind Vadakkayil: technique; David H. Waldeck: conceptualization, project administration, supervision, writing – review & editing.

Conflicts of interest

The authors declare that they have no known competing financial interests or personal relationships that could have appeared to influence the work reported in this paper.

Data availability

The data supporting this article has been included as part of the supplementary information (SI). The supporting information includes initial characterizations of polyaniline spin transport layer (thickness calibration and I–V curves from mcAFM measurements), characterizations of catalyst deposited platform (XPS, SEM, CD and electrochemical data), electrochemical data of R-PANI vs. racemic PANI (linear sweep voltammetry and Tafel plots), comparison of S-PANI vs. R-PANI chiral spin transport layer, double layer capacitance measurements and iR compensation data. See DOI: https://doi.org/10.1039/d5ta04850h.

Acknowledgements

References

1 Y. J. Wang, D. P. Wilkinson and J. Zhang, *Chem. Rev.*, 2011, **111**, 7625–7651.

2 P. Boldrin, E. Ruiz-Trejo, J. Mermelstein, J. M. Bermúdez Menéndez, T. Ramírez Reina and N. P. Brandon, *Chem. Rev.*, 2016, **116**, 13633–13684.

3 G. M. Whitesides and G. W. Crabtree, *Science*, 2007, **315**, 796–798.

4 N. T. Suen, S. F. Hung, Q. Quan, N. Zhang, Y. J. Xu and H. M. Chen, *Chem. Soc. Rev.*, 2017, **46**, 337–365.

5 S. Chretien and H. Metiu, *J. Chem. Phys.*, 2008, **129**, 074705.

6 H. Dau, C. Limberg, T. Reier, M. Risch, S. Roggan and P. Strassser, *ChemCatChem*, 2010, **2**, 724–761.

7 M. Che, *Catal. Today*, 2013, **218**, 162–171.

8 J. Rossmeisl, Z.-W. Qu, H. Zhu, G.-J. Kroes and J. K. Nørskov, *J. Electroanal. Chem.*, 2007, **607**, 83–89.

9 I. C. Man, H. Y. Su, F. Calle-Vallejo, H. A. Hansen, J. I. Martínez, N. G. Inoglu, J. Kitchin, T. F. Jaramillo, J. K. Nørskov and J. Rossmeisl, *ChemCatChem*, 2011, **3**, 1159–1165.

10 J. Qian, T. Wang, Z. Zhang, Y. Liu, J. Li and D. Gao, *Nano Energy*, 2020, **74**, 104948.

36726 | *J. Mater. Chem. A*, 2025, **13**, 36720–36728

This journal is © The Royal Society of Chemistry 2025

11 J. Ran, T. Wang, J. Zhang, Y. Liu, C. Xu, S. Xi and D. Gao, *Chem. Mater.*, 2020, **32**, 3439–3446.

12 J. Ran, L. Wang, M. Si, X. Liang and D. Gao, *Small*, 2023, **19**, 2206367.

13 R. M. Ramsundar, V. K. Pillai and P. A. Joy, *Phys. Chem. Chem. Phys.*, 2018, **20**, 29452–29461.

14 X. Ren, T. Wu, Y. Sun, Y. Li, G. Xian, X. Liu, C. Shen, J. Gracia, H. J. Gao and H. Yang, *Nat. Commun.*, 2021, **12**, 2608.

15 T. Wu, X. Ren, Y. Sun, S. Sun, G. Xian, G. G. Scherer, A. C. Fisher, D. Mandler, J. W. Ager and A. Grimaud, *Nat. Commun.*, 2021, **12**, 3634.

16 T. Wu and Z. J. Xu, *Curr. Opin. Electrochem.*, 2021, **30**, 100804.

17 X. Ren, T. Wu, Z. Gong, L. Pan, J. Meng, H. Yang, F. B. Dagbjartsdottir, A. Fisher, H.-J. Gao and Z. J. Xu, *Nat. Commun.*, 2023, **14**, 2482.

18 F. A. Garces-Pineda, M. Blasco-Ahicart, D. Nieto-Castro, N. Lopez and J. R. Galan-Mascaros, *Nat. Energy*, 2019, **4**, 519–525.

19 C. Hunt, Z. Zhang, K. Ocean, R. P. Jansonius, M. Abbas, D. J. Dvorak, A. Kurimoto, E. W. Lees, S. Ghosh, A. Turkiewicz, F. A. Garces Pineda, D. K. Fork and C. P. Berlinguette, *J. Am. Chem. Soc.*, 2022, **144**, 733–739.

20 A. Karmakar, D. Mahendrian, R. Madhu, P. Murugan and S. Kundu, *J. Mater. Chem. A*, 2023, **11**, 16349.

21 S. Nagappan, A. Karmakar, R. Madhu, S. S. Selvasundarasekar, S. Kumarevel, K. Bera, H. N. Dhandapani, D. Sarkar, S. M. Yusuf and S. Kundu, *ACS Appl. Energy Mater.*, 2022, **5**, 11483.

22 W. Zhang, K. B. Ghosh, F. Tassinari and R. Naaman, *ACS Energy Lett.*, 2018, **3**, 2308–2313.

23 S. Ghosh, B. P. Bloom, Y. Lu, D. Lamont and D. H. Waldeck, *J. Phys. Chem. C*, 2020, **124**, 22610–22618.

24 K. B. Ghosh, W. Zhang, F. Tassinari, Y. Mastai, O. Lidor-Shalev, R. Naaman, P. Möllers, D. Nurenberg, H. Zacharias and J. Wei, *J. Phys. Chem. C*, 2019, **123**, 3024–3031.

25 A. N. Nair, S. Fernandez, M. Marcos-Hernández, D. R. Romo, S. R. Singamaneni, D. Villagran and S. T. Sreenivasan, *Nano Lett.*, 2023, **23**, 9042–9049.

26 A. Vadakkayil, C. Clever, K. N. Kunzler, S. Tan, B. P. Bloom and D. H. Waldeck, *Nat. Commun.*, 2023, **14**, 1067.

27 P. K. Bhartiya, M. Srivastava and D. Mishra, *Int. J. Hydrogen Energy*, 2021, **47**, 42160–42170.

28 J. Meng, H. Li, R. Chen, X. Sun and X. Sun, *ChemPlusChem*, 2019, **84**, 1816–1822.

29 W. Zhang, W. Wang, Y. Hu, H. Guan and L. Hao, *Int. J. Hydrogen Energy*, 2021, **46**, 3504–3509.

30 Y. Liang, M. Lihter and M. Lingenfelder, *Isr. J. Chem.*, 2022, **62**, e202200052.

31 P. Vensaus, Y. Liang, N. Zigon, N. Avarvari, V. Mujica, G. J. Soler-Illia and M. J. Lingenfelder, *Chem. Phys.*, 2024, **160**, 111103.

32 D. Barik, U. Utkarsh and K. B. Ghosh, *Chem. Commun.*, 2025, **61**, 6226–6245.

33 W. Mtangi, V. Kiran, C. Fontanesi and R. Naaman, *J. Phys. Chem. Lett.*, 2015, **6**, 4916–4922.

34 W. Mtangi, F. Tassinari, K. Vankayala, A. Vargas Jentzsch, B. Adelizzi, A. R. Palmans, C. Fontanesi, E. W. Meijer and R. Naaman, *J. Am. Chem. Soc.*, 2017, **139**, 2794–2798.

35 F. Tassinari, K. B. Ghosh, F. Parenti, V. Kiran, A. Mucci and R. Naaman, *J. Phys. Chem. C*, 2017, **121**, 15777–15783.

36 A. Vadakkayil, W. A. Dunlap-Shohl, M. Joy, B. P. Bloom and D. H. Waldeck, *ACS Catal.*, 2024, **14**, 17303–17309.

37 H. Gajapathy, S. Bandaranayake, E. Hruska, A. Vadakkayil, B. P. Bloom, S. Londo, J. McClellan, J. Guo, D. Russell, F. M. de Groot and F. Yang, *Chem. Sci.*, 2024, **15**, 3300–3310.

38 L. Pan, M. Ai, C. Huang, L. Yin, X. Liu, R. Zhang, S. Wang, Z. Jiang, X. Zhang, J. J. Zou and W. Mi, *Nat. Commun.*, 2020, **11**, 418.

39 B. Fang, Z. Xing, W. Kong, Z. Li and W. Zhou, *Nano Energy*, 2022, **101**, 107616.

40 Y. Liang, K. Banjac, K. Martin, N. Zigon, S. Lee, N. Vanthuyne, F. A. Garcés-Pineda, J. R. Galán-Mascarós, X. Hu, N. Avarvari and M. Lingenfelder, *Nat. Commun.*, 2022, **13**, 3356.

41 L. L. Hao, J. Y. Hu, J. Li, Y. J. Gao, Y. S. Meng and T. Liu, *ACS Catal.*, 2025, **15**, 5640–5650.

42 H. Li, Q. Quan, C. Y. Wong and J. C. Ho, *Adv. Energy Sustain. Rev.*, 2025, **6**, 2400326.

43 E. Van der Minne, P. Vensaus, V. Ratovskii, S. Hariharan, J. Behrends, C. Franchini, J. Fransson, S. S. Dhesi, F. Gunkel, F. Gossing, G. Katsoukis, U. I. Kramm, M. Lingenfelder, Q. Lan, Y. V. Kolen'Ko, Y. Li, R. R. Mohan, J. McCord, L. Ni, E. Pavarini, R. Pentcheva, D. H. Waldeck, M. Verhage, A. Yu, Z. I. Xu, P. Torelli, S. Mauri, N. Avarvari, A. Bieberle-Huetter and C. Baeumer, *Adv. Energy Mater.*, 2025, in press.

44 X. Chen, Y. Chen, Z. Shen, C. Song, P. Ji, N. Wang, D. Su, Y. Wang, G. Wang and L. Cui, *Appl. Surf. Sci.*, 2020, **529**, 147173.

45 X. Sun, X. Liu, R. Liu, X. Sun, A. Li and W. Li, *Catal. Commun.*, 2020, **133**, 105826.

46 X. Zou, Q. Lu, M. Tang, J. Wu, K. Zhang, W. Li, Y. Hu, X. Xu, X. Zhang, Z. Shao and L. An, *Nano–Micro Lett.*, 2025, **17**, 6.

47 L. Jia, C. Wang, Y. Zhang, L. Yang and Y. Yan, *ACS Nano*, 2020, **14**, 6607–6615.

48 S. Mishra, A. Kumar, M. Venkatesan, L. Pigani, L. Pasquali and C. Fontanesi, *Small Methods*, 2020, **4**, 2000617.

49 S. Mishra, E. G. Bowes, S. Majumder, J. A. Hollingsworth, H. Htoon and A. C. Jones, *ACS Nano*, 2024, **18**, 8663–8672.

50 M. Al-Gharram, I. Jum'h, A. Telfah and M. Al-Hussein, *Colloids Surf.*, 2021, **628**, 127342.

51 C. T. P. da Silva, V. L. Kupfer, G. R. da Silva, M. P. Moisés, M. A. G. Trindade, N. L. de Campos Domingues and A. W. Rinaldi, *Int. J. Electrochem. Sci.*, 2016, **11**, 5380–5394.

52 O. Belgherbi, D. Chouder and M. A. Saeed, *Optik*, 2018, **171**, 589–599.

53 M. Al-Gharram and T. AlZoubi, *Ceram. Int.*, 2024, **50**, 5473–5482.

54 K. Michaeli, V. Varade, R. Naaman and D. H. Waldeck, *J. Phys.: Condens. Matter*, 2016, **29**, 103002.

This journal is © The Royal Society of Chemistry 2025

J. Mater. Chem. A, 2025, **13**, 36720–36728 | **36727**

55 A. Kumar, E. Capua, M. K. Kesharwani, J. M. L. Martin, E. Sitbon, D. H. Waldeck and R. Naaman, *Proc. Natl. Acad. Sci.*, 2017, **114**, 2474.

56 M. Eckshtain-Levi, E. Capua, S. Refaely-Abramson, S. Sarkar, Y. Gavrilov, S. P. Mathew, Y. Paltiel, Y. Levy, L. Kronik and R. Naaman, *Nat. Commun.*, 2016, **7**, 10744.

57 J. Lyskawa and D. Bélanger, *Chem. Mater.*, 2006, **18**, 4755–4763.

58 W. Ullah, G. Herzog, N. Vilà and A. Walcarius, *Electrochem. Commun.*, 2021, **122**, 106896.

59 N. F. Heinig, N. Kharbanda, M. R. Pynenburg, X. J. Zhou, G. A. Schultz and K. T. Leung, *Mater. Lett.*, 2008, **62**, 2285–2288.

60 X. J. Zhou, A. J. Harmer, N. F. Heinig and K. T. Leung, *Langmuir*, 2004, **20**, 5109–5113.

61 W. S. Huang and A. G. MacDiarmid, *Polymer*, 1993, **34**, 1833–1845.

62 R. Dubey, D. Dutta and P. Chattopadhyay, *Polym. Bull.*, 2024, **81**, 8547–8571.

63 C. Clever, E. Wierzbinski, B. P. Bloom, Y. Lu, H. M. Grimm, S. R. Rao, W. S. Horne and D. H. Waldeck, *Isr. J. Chem.*, 2022, **62**, e202200045.

64 B. P. Bloom, V. Kiran, V. Varade, R. Naaman and D. H. Waldeck, *Nano Lett.*, 2016, **16**, 4583–4589.

65 F. Song, M. M. Busch, B. Lassalle-Kaiser, C. S. Hsu, E. Petkucheva, M. Bensimon, H. M. Chen, C. Corminboeuf and X. Hu, *ACS Cent. Sci.*, 2019, **5**, 558–568.

66 M. Retuerto, L. Pascual, F. Calle-Vallejo, P. Ferrer, D. Gianolio, A. G. Pereira, Á. García, J. Torrero, M. T. Fernández-Díaz, P. Bencok and M. A. Peña, *Nat. Commun.*, 2019, **10**, 2041.

67 K. B. Ghosh, W. Zhang, F. Tassinari, Y. Mastai, O. Lidor-Shalev, R. Naaman, P. Mollers, D. Nurenberg, H. Zacharias, J. Wei and E. Wierzbinski, *J. Phys. Chem. C*, 2019, **123**, 3024–3031.

68 L. F. Huang, M. J. Hutchison, R. J. Santucci Jr, J. R. Scully and J. M. Rondinelli, *J. Phys. Chem. C*, 2017, **121**, 9782–9789.

69 L. F. Huang and J. M. Rondinelli, *npj Mater. Degrad.*, 2019, **3**, 26.

70 J. Chivot, L. Mendoza, C. Mansour, T. Pauporté and M. Cassir, *Corros. Sci.*, 2008, **50**, 62–69.

71 M. Bajdich, M. García-Mota, A. Vojvodic, J. K. Nørskov and A. T. Bell, *J. Am. Chem. Soc.*, 2013, **135**, 13521–13530.

72 W. Luo, C. Jiang, Y. Li, S. A. Shevlin, X. Han, K. Qiu, Y. Cheng, Z. Guo, W. Huang and J. Tang, *J. Mater. Chem. A*, 2017, **5**, 2021–2028.

73 R. Swierk, S. Klaus, L. Trotochaud, A. T. Bell and T. D. J. Tilley, *J. Phys. Chem. C*, 2015, **119**, 19022–19029.

74 S. Song, H. Bao, X. Lin, X. L. Du, J. Zhou, L. Zhang, N. Chen, J. Hu and J. Q. Wang, *J. Energy Chem.*, 2020, **42**, 5–10.

75 X. Liu, S. Cui, Z. Sun, Y. Ren, X. Zhang and P. Du, *J. Phys. Chem. C*, 2016, **120**, 831–840.

76 X. Liu, H. Jia, Z. Sun, H. Chen, P. Xu and P. Du, *Electrochem. Commun.*, 2014, **46**, 1–4.

77 M. R. Gao, X. Cao, Q. Gao, Y. F. Xu, Y. R. Zheng, J. Jiang and S. H. Yu, *ACS Nano*, 2014, **8**, 3970–3978.

78 M. Retuerto, L. Pascual, F. Calle-Vallejo, P. Ferrer, D. Gianolio, A. G. Pereira, Á. García, J. Torrero, M. T. Fernández-Díaz, P. Bencok and M. A. Peña, *Nat. Commun.*, 2019, **10**, 2041.

79 X. Ren, T. Wu, Y. Sun, Y. Li, G. Xian, X. Liu, C. Shen, J. Gracia, H. J. Gao, H. Yang and Z. J. Xu, *Nat. Commun.*, 2021, **12**, 2608.

80 T. Wu and Z. J. Xu, *Curr. Opin. Electrochem.*, 2021, **30**, 100804.

81 K. Shiota, A. Inui, Y. Hosaka, R. Amano, Y. Ōnuki, M. Hedo, T. Nakama, D. Hirobe, J. I. Ohe, J. I. Kishine and H. M. Yamamoto, *Phys. Rev. Lett.*, 2021, **127**, 126602.

82 H. Shishido, R. Sakai, Y. Hosaka and Y. Togawa, *Appl. Phys. Lett.*, 2021, **119**, 182403.

36728 | *J. Mater. Chem. A*, 2025, **13**, 36720–36728

This journal is © The Royal Society of Chemistry 2025